A *W*-Band SPDT Photoconductive Evanescent-Mode Waveguide Switch

Eric T. Der, *Graduate Student Member, IEEE*, Thomas R. Jones, *Member, IEEE*, Alden Fisher, *Graduate Student Member, IEEE*, Michael D. Sinanis, *Member, IEEE*, Kambiz Moez, *Senior Member, IEEE*, Douglas W. Barlage, *Senior Member, IEEE*, and Dimitrios Peroulis, *Fellow, IEEE*

***Abstract*— This letter presents the design, fabrication, and measurement of a silicon micromachined photoconductive evanescent (EVA)-mode waveguide switch operating in a single-pole double-throw (SPDT) configuration. Two EVA-mode waveguides loaded with silicon posts are placed in a Y configuration with a common feeding waveguide. In the absence of photoexcitation, the dielectric posts and EVA channel exhibit a bandpass filter response that allows low-loss propagation of signals on the order of 2.0 dB at 96.7 GHz. When photoexcited, the low conductive posts and EVA channel yield a very high isolation of 36.5 dB up to 102.4 GHz within *W*-band. The proposed design shows promise for 5G and 6G communication backhaul devices.**

***Index Terms*— 5G, 6G, evanescent (EVA) mode, millimeter wave (mmWave), photoconductive switch, silicon micromachining, waveguide.**

I. Introduction

TO MEET the growing demands for connectivity and higher data rates, the fifth generation (5G) of wireless communication systems is expanding into the millimeter wave (mmWave) domain where spectrum is—for the most part—in abundance. However, the utilization of these higher frequency signals presents unique challenges, such as higher path losses, higher atmospheric attenuation, and greater radiation losses from conventional planar microwave transmission lines, such as microstrip [1] and coplanar waveguides [2].

Moving forward, sixth generation (6G) systems are expected to utilize spectrum in the *W*-band where the aforementioned challenges are further amplified [3]; this requires the development of waveguide interconnects, which have been shown to have relatively low insertion losses (ILs) up to several hundreds of GHz [4]. In mmWave switch technologies, p-i-n diodes, electromechanical switches, and RF MEMS have all been integrated into waveguide-based interconnects. However, electromechanical switches have slow switching speeds, RF MEMS has reliability issues and higher production costs compared with semiconductors, and mmWave p-i-n diodes generally have low power handling and high ILs [5].

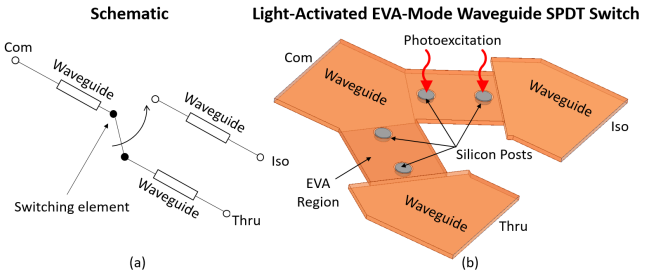

Fig. 1. Illustrations of SPDT switches. (a) General schematic of SPDT switches, which consist of a "common" port that is always connected to one of two other branches. The port currently connected to the common port is known as the "through/thru" port, and the disconnected one, the "isolated" port. (b) General concept of an SPDT switch using the photoconductive waveguide switch technology. The channel that is not excited with light behaves like a bandpass filter, whereas the photoexcited branch is shorted and is isolated from the common port.

Photoconductive waveguide switches, on the other hand, have been shown to be an excellent compromise between the high switching speeds of semiconductor switches while offering relatively high power handling [6]. Furthermore, they have been shown to offer low IL and have high linearity. In [7], it has been shown that the optical power needed to achieve high isolation using photoconductive silicon posts can be reduced by placing them in evanescent (EVA)-mode waveguide channels, albeit sacrificing some bandwidth.

Multithrow switches play a key role in RF communication frontends, such as reconfigurable antennas [8], Rotman lenses [9], and Butler matrices [10], [11], which require common source signals to be routed to different channels robustly. Here, a single-pole double-throw (SPDT) photoconductive EVA-mode switch is designed, analyzed, fabricated, and measured.

II. Principle of Operation

Fig. 1 depicts the fundamental concept of a photoconductive EVA-mode SPDT waveguide switch. The EVA region of a waveguide channel has a higher cutoff frequency, which does not normally allow propagation of electromagnetic waves, and has been shown in the literature to behave as an inductive π or T network [12]. However, the addition of silicon dielectric posts is equivalent to placing a shunt capacitor. Together, this combination of reactive impedances, i.e., a shunt inductor from the EVA region along with a shunt capacitor from the silicon

Manuscript received 28 February 2023; revised 11 April 2023; accepted 15 April 2023. Date of publication 3 May 2023; date of current version 7 June 2023. This work was supported in part by the Canadian Department of National Defence, in part by the National Research Council of Canada Industrial Research Assistance Program, in part by CMC Microsystems, and in part by Jones Microwave Inc. *(Corresponding author: Eric T. Der.)*

Eric T. Der, Kambiz Moez, and Douglas W. Barlage are with the Department of Electrical and Computer Engineering, University of Alberta, Edmonton, AB T6G 1H9, Canada (e-mail: der@ualberta.ca).

Thomas R. Jones, Alden Fisher, Michael D. Sinanis, and Dimitrios Peroulis are with the Elmore Family School of Electrical and Computer Engineering, Purdue University, West Lafayette, IN 47907 USA.

This article was presented at the IEEE MTT-S International Microwave Symposium (IMS 2023), San Diego, CA, USA, June 11–16, 2023.

Color versions of one or more figures in this letter are available at https://doi.org/10.1109/LMWT.2023.3268947.

Digital Object Identifier 10.1109/LMWT.2023.3268947

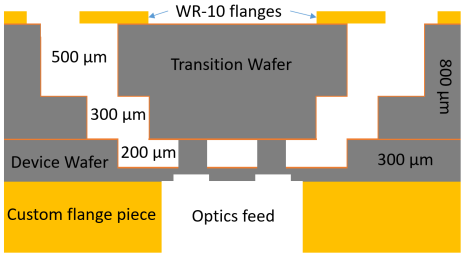

Fig. 2. Longitudinal cross section of the proposed silicon micromachined EVA-mode waveguide switch. A 200-μm-deep cavity is etched into a 300-μm HR-Si wafer to form the EVA channel and posts. Two cavities (500- and 300-μm deep) are etched in an 800-μm wafer to form an E-plane bend transition that matches the impedance of the 200-μm-high waveguide channel on the device layer to that of the standard WR-10 waveguides. A custom laser cut flange piece is screwed on to the WR-10 flange connectors to mechanically bind the 300-μm device wafer on to the 800-μm transition wafer.

post, resonates resulting in a bandpass filter response [13] between the common and thru ports when the high-resistivity silicon (HR-Si) posts are in their unexcited states (ON-state). In the isolated branch where Si posts are excited with light, the combination of a waveguide operating in cutoff coupled with low-impedance shunts to ground yields very high switch isolations.

The fundamental operating principle behind the proposed switch is the photoconductive effect. Here, conductivity can be induced in a semiconductor through light excitation at a photon energy greater than the bandgap of the semiconductor, generating electron–hole pairs inside the material. HR-Si is a good candidate for the switching element due to its ability to act as a low-loss dielectric at the mmWave band in the absence of photoexcitation. Furthermore, its relatively low bandgap offers an abundance of high-power optics solutions for inducing high conductivity. The dc conductivity of silicon can be computed as follows [5], [14]:

$$\sigma_{\mathrm{dc}} = q(\mu_p + \mu_n)n' \tag{1}$$

where q is the elementary charge, n' is the excess carrier concentration (assumed to be uniform in the material), and μ_n and μ_p are the carrier mobilities of electrons and holes, respectively. It can be seen that conductivity is dependent on n', which can, in turn, be computed as a function of photoexcitation as follows [5], [14]:

$$n' = \frac{P_0/h\nu}{\alpha H^2}\tau(n')(1-R)\left(1-e^{-\alpha H}\right) \tag{2}$$

where P_0 is the incident light intensity, R and α are, respectively, the reflection and absorption coefficients of the material, τ the carrier lifetime, and H the height of the semiconducting material under excitation. It can be seen from (1) and (2) that the conductivity of the silicon switching elements increases with optical power. Loading the center of a rectangular waveguide, the HR-Si posts can be used to route the RF signals [5]. When excited with photons above the bandgap energy of silicon ($E_g = 1.12$ eV), the HR-Si posts enter their conductive state and short the TE_{10} mode where it is strongest. When no light is present, the HR-Si low-loss dielectric allows RF propagation through the waveguide.

III. Design

With the fundamental scientific principles that enable the operation of the proposed design established, this section introduces the design process details of an SPDT silicon photoconductive waveguide switch. Fig. 2 depicts the transverse cross section of the proposed switch technology. The device is fabricated on a 200-μm-high waveguide channel etched into a silicon wafer (device wafer), which is then binded onto an 800-μm silicon transition wafer using mechanical pressure via screws. Fig. 1 depicts the schematic of a waveguide SPDT switch. In the OFF/isolated-state of a channel (no RF signal propagation), the silicon posts in that branch are made conductive by photon stimulation in an optical wavelength region of high quantum efficiency (915 nm) [14], shorting any RF signal attempting to pass through to ground.

A. Study of 120° Y-Junctions With Shunt Short-Circuited Stubs

Owing to its relatively shallow bend, the waveguide Y-junction has relatively low loss and has, therefore, been one of the most popular methods to branch microwave interconnects [15]. The proposed SPDT switch design operates by connecting or disconnecting one of the two Y-junction output branches with the common waveguide feed. In this section, we discuss the optimal placement of the switching elements in the Y-junction to maximize the bandwidth of the SPDT switch.

In the literature, it is common for the shunt shorting element of multithrow TEM transmission line-based switches to be placed $\lambda/4$ away from the junction to prevent shorting out the TEM mode. In contrast, an open-circuit boundary at the Y-junction of a waveguide-based switch will result in a discontinuity to its fundamental TE_{10} mode; therefore, the shorting element must be placed $\lambda/2$ away from the junction to provide the mode with an electric "sidewall" [16].

However, $\lambda/2$ impedance transformers do not maintain 180° phase over a wide frequency band, resulting in narrowband responses and stopbands. Since a short-circuited $\lambda/2$ stub results in a low-impedance boundary at the input reference plane, we can introduce a simplified design where a low-impedance switching element is placed right against the Y-junction. By removing the short-circuited stub and placing the PEC boundary right against the junction, the model is effectively reduced to a simple waveguide bend, and a good impedance match and transmission can be maintained over a wide band owing to the absence of resonating structures [17]. Fig. 3 shows the simulated impedance of a reflected signal from an OFF-state EVA channel where the posts are made conductive via laser excitation; it can clearly be seen that an EVA-mode switch in its OFF-state resembles a low-impedance boundary. It can, therefore, be inferred that the bandwidth of the proposed SPDT switch can be maximized by placing the individual EVA-mode switching elements as close to the Y-junction as possible.

B. SPDT Switch Design With E-Plane Bend Transitions

With the theoretical basis of optimizing a switched waveguide Y-junction established, we can now integrate the standalone silicon photoconductive EVA-mode waveguide switch into the proposed SPDT configuration. To fully take advantage of the low propagation loss of the waveguide switch technology at W-band and beyond, it is prudent that the entire system be fed and interconnected purely with waveguide structures. This proposed switch is fed with standard WR-10 waveguides.

Fig. 4 depicts an SPDT EVA-mode switch with an E-plane bend to be constructed from stacked silicon wafers [18], which also serves as an impedance transformer for interfacing a WR-10 waveguide flange to the 200-μm-high channel the switch is constructed in. The impedance match can be optimized by tuning the step widths (a_0 and a_1), step lengths

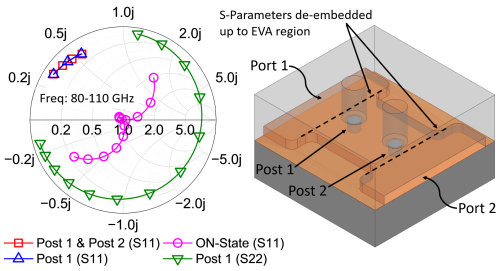

Fig. 3. Simulated reflection coefficients of a single-throw EVA-mode waveguide switch de-embedded up to the EVA section, with different combinations of posts excited by light. When both posts are excited, the S_{11} response indicates a low-impedance boundary (likewise S_{22} due to symmetry). When only post 1 is excited, S_{11} indicates a low-impedance boundary, whereas S_{22} indicates a high-impedance boundary. The ON-state with no posts excited indicates good impedance matching, as expected.

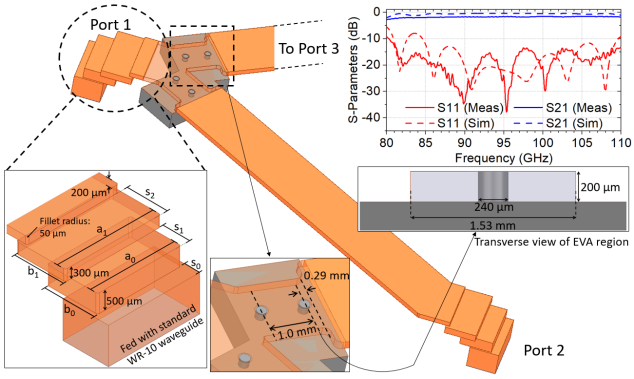

Fig. 4. 3-D model of a two-pole photoconductive EVA-mode SPDT switch. By exciting the switch posts on the identical branches connected to ports 2 and 3, one can determine which branch to cutoff RF signal propagation to from the common port (port 1). The three E-plane bend transitions have identical dimensions, where $s_0 = 0.35$ mm, $s_1 = 0.74$ mm, $s_2 = 1.2$ mm, $a_0 = 2.4$ mm, $a_1 = 2.8$ mm, $b_0 = 1.39$ mm, and $b_1 = 1.35$ mm. The graph shows the simulated and measured data of a 20.75-mm line with the E-bend transitions that branch off at the same angle as the proposed switch.

(b_0 and b_1), and the offsets among the steps (s_0, s_1, and s_2) in the propagating direction. In this design, the common waveguide feed (port 1) is directly branched off into two EVA-mode channels at an angle of 67.8°. The silicon posts in the port-3 branch were simulated with a conductivity of 425 S/m to emulate its photoexcited state, not allowing microwave propagation. Port 2 is the through port in the simulation; its silicon posts are not excited and are assumed to have a conductivity of 0.1 S/m (for 1-k$\Omega \cdot$ cm HR-Si wafers). The arms on ports 2 and 3 must be extended by 15.5 mm in order to fit the UG-387/U flange connectors. The measured peak IL of the transitions with a 20.75-mm length of line is 1.6 dB.

IV. Fabrication

Fig. 5 depicts the fabrication process flow for the proposed device. Deep reactive ion etching (DRIE) is used on a 300-μm HR-Si wafer (device wafer) to form the waveguide channel and posts on the front side (FS) as well as the optical fiber feed holes on the backside (BS) and through holes for aligning standard UG-387/U flange connectors. A second 800-μm Si wafer (transition wafer) is also etched using DRIE on both sides to form the two steps of the E-plane bend transition and the through holes for the flange connectors. Both wafers are metalized with 80 nm of titanium for adhesion, 1.2 μm of copper, and 25 nm of gold to prevent oxidation. In measurements, the two wafers are sandwiched and tightened with screws that are torqued onto the flange connectors and a custom laser machined metal flange piece.

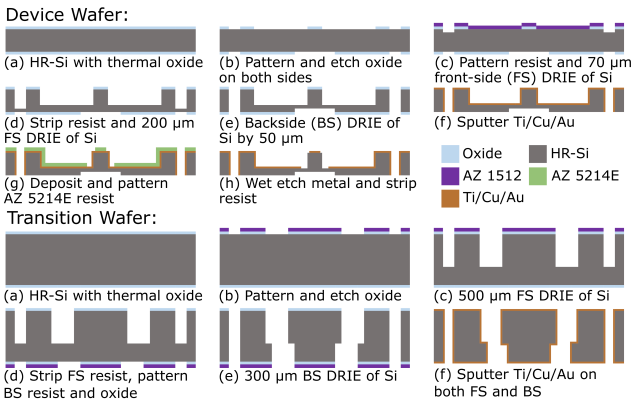

Fig. 5. Fabrication process flow for the SPDT device wafer (switching channel) and the transition wafer (E-plane bend). (a) HR-Si with thermal oxide. (b) Pattern and etch oxide on both sides. (c) Pattern resist and 70-μm FS DRIE of Si. (d) Strip resist and 200-μm FS DRIE of Si. (e) BS DRIE of Si by 50 μm. (f) Sputter Ti/Cu/Au. (g) Deposit and pattern AZ 5214E resist. (h) Wet etch metal and strip resist. (i) HR-Si with thermal oxide. (j) Pattern resist and etch oxide. (k) 500-μm FS DRIE of Si. (l) Strip FS resist, pattern BS resist and oxide. (m) 300-μm BS DRIE of Si. (n) Sputter Ti/Cu/Au on both FS and BS.

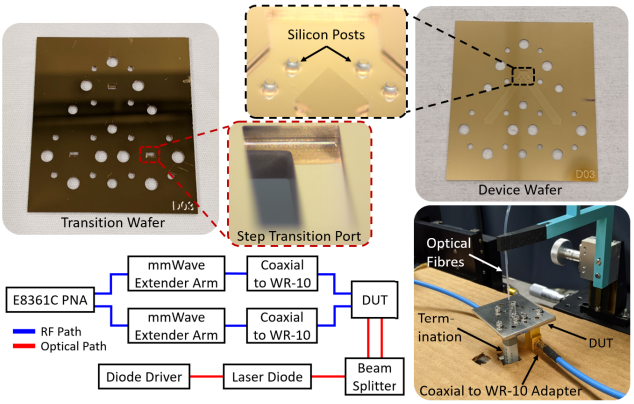

Fig. 6. Block diagram and photographs of the experimental setup/DUT for measuring the S-parameters of the fabricated devices described in Section II. The N5260 extender modules allow for RF characterization up to 110 GHz. An adapter is used to interface the 1.0-mm coaxial output from the extender modules to the WR-10 connectors on the DUT. The optical setup uses a Wavelength Electronics LD5CHA laser diode driver, a 915-nm laser diode from Sheaumann Laser Inc., an OZ Optics nonpolarizing beam splitter, and two 400/440-μm multimode fibers.

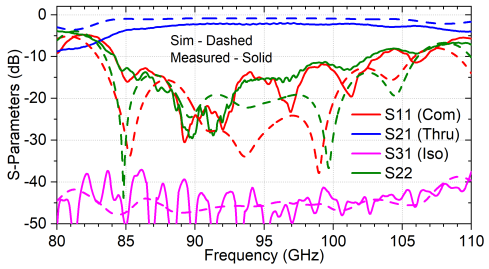

Fig. 7. Measured and simulated results of the proposed photoconductive SPDT waveguide switch for both the thru and isolated branches.

V. Results and Discussion

The block diagram and photograph of the experimental setup for characterizing the S-parameters of the proposed switch are shown in Fig. 6. Frequency extender modules are used to allow small-signal characterization up to 110 GHz. Fiber optic cables are landed on the chip after the 1.0-mm coaxial to WR-10 adapters is torqued on to the device under test (DUT). The measured ON-state S-parameters of the two-pole SPDT switch with the laser switched off, and the

TABLE I
COMPARISON OF THE PROPOSED SPDT SWITCH TO THE EXISTING TECHNOLOGIES

Ref.	Technology	Frequency Range (GHz)	10-dB RL FBW (%)	Peak IL (dB)	Isol. (dB)
This Work	Photoconductive Si (Waveguide)	84.3–102.4[a]	19.4[a]	2.0[a]	36.5[a]
[16]	Photoconductive Si (SIW)	74 – 85.8	15	2.2	30
[17]	PIN Diode (SIW)	7.0 – 10.2	37	2.1	10

[a] Results reported include transition losses.

OFF-state, with the laser switched on, are shown in Fig. 7. The device is able to achieve a 10-dB return loss (RL) bandwidth spanning 84.3–102.4 GHz with a peak thru IL of 2.0 dB at 96.7 GHz and a minimum isolation of 36.5 dB using 582 mW of total optical power. Using just 187 mW of optical excitation, a 35-dB isolation can be maintained with only an additional 0.2-dB IL added, a significant benefit of the EVA-mode switch. Compared with the measured transition line in Fig. 4, it can be seen that the SPDT switch itself only adds 0.4-dB IL.

In Table I, the proposed device is compared with other integrated waveguide SPDT switches. The proposed design shows the lowest IL (even with transition losses included) at the highest frequency band and also achieves the highest isolation. Furthermore, an in-line transition in future implementations can reduce the length of line needed and further reduce the total IL.

VI. CONCLUSION

The design and experimental results of a *W*-band silicon micromachined photoconductive EVA-mode waveguide SPDT switch were presented. Between 85 and 100 GHz, the maximum IL was shown to be 2.0 dB at 96.7 GHz, and a minimum isolation of 36.5 dB was achieved between the common and isolated ports. The results show promise for the proposed switch to be used in 5G and 6G communications.

ACKNOWLEDGMENT

Part of this work was conducted at the nanoFAB Centre, University of Alberta, Edmonton, AB, USA. Thomas Jones would like to thank Dr. Michael Finot and Dr. Pedro Duarte of Rocky Mountain Micro Machining (RM3) for their help with fabrication of the devices.

REFERENCES

[1] A. Sabban and K. C. Gupta, "Characterization of radiation loss from microstrip discontinuities using a multiport network modeling approach," *IEEE Trans. Microw. Theory Techn.*, vol. 39, no. 4, pp. 705–712, Apr. 1991.

[2] F.-L. Lin and R.-B. Wu, "Computations for radiation and surface-wave losses in coplanar waveguide bandpass filters," *IEEE Trans. Microw. Theory Techn.*, vol. 47, no. 4, pp. 385–389, Apr. 1999.

[3] G. Wikstrom et al., "Challenges and technologies for 6G," in *Proc. 2nd 6G Wireless Summit (6G SUMMIT)*, Mar. 2020, pp. 1–5.

[4] A. Krivovitca, U. Shah, O. Glubokov, and J. Oberhammer, "Micromachined silicon-core substrate-integrated waveguides with co-planarprobe transitions at 220–330 GHz," in *IEEE MTT-S Int. Microw. Symp. Dig.*, Jun. 2018, pp. 190–193.

[5] T. R. Jones, A. Fisher, D. W. Barlage, and D. Peroulis, "A photogenerated silicon plasma waveguide switch and variable attenuator for millimeter-wave applications," *IEEE Trans. Microw. Theory Techn.*, vol. 69, no. 12, pp. 5393–5403, Dec. 2021.

[6] A. Fisher, Z. V. Missen, T. R. Jones, and D. Peroulis, "A fiber-free DC-7 GHz 35 W integrated semiconductor plasma switch," in *IEEE MTT-S Int. Microw. Symp. Dig.*, Atlanta, GA, USA, Jun. 2021, pp. 27–30.

[7] T. R. Jones, A. Fisher, D. W. Barlage, and D. Peroulis, "A W-band photoconductive evanescent-mode waveguide switch," in *IEEE MTT-S Int. Microw. Symp. Dig.*, Denver, CO, USA, Jun. 2022, pp. 959–962.

[8] Y. Chen, L. Zhang, Y. He, W. Li, and S.-W. Wong, "A pattern reconfigurable SIW horn antenna realized by PIN diode switches," in *Proc. Comput., Commun. IoT Appl. (ComComAp)*, Shenzhen, China, Nov. 2021, pp. 112–115.

[9] Y. Gao, M. Khaliel, F. Zheng, and T. Kaiser, "Rotman lens based hybrid analog–digital beamforming in massive MIMO systems: Array architectures, beam selection algorithms and experiments," *IEEE Trans. Veh. Technol.*, vol. 66, no. 10, pp. 9134–9148, Jun. 2017.

[10] E. T. Der, T. R. Jones, and M. Daneshmand, "Miniaturized 4 × 4 Butler matrix and tunable phase shifter using ridged half-mode substrate integrated waveguide," *IEEE Trans. Microw. Theory Techn.*, vol. 68, no. 8, pp. 3379–3388, Aug. 2020.

[11] E. T. Der, T. R. Jones, and M. Daneshmand, "A miniaturized 28 GHz 4 × 4 Butler matrix using shielded ridged half-mode SIW," in *IEEE MTT-S Int. Microw. Symp. Dig.*, Atlanta, GA, USA, Jun. 2021, pp. 776–779.

[12] G. F. Craven and C. K. Mok, "The design of evanescent mode waveguide bandpass filters for a prescribed insertion loss characteristic," *IEEE Trans. Microw. Theory Techn.*, vol. MTT-19, no. 3, pp. 295–308, Mar. 1971.

[13] R. J. Cameron, C. M. Kudsia, and R. R. Mansour, *Microwave Filters for Communication Systems*. Hoboken, NJ, USA: Wiley, Mar. 2018.

[14] S. Sze and K. K. Ng, *Physics of Semiconductor Devices*. Hoboken, NJ, USA: Wiley, 2006.

[15] H. Chen, W. Che, T. Zhang, Y. Chao, and W. Feng, "SIW SPDT switch based on switchable HMSIW units," in *Proc. IEEE Int. Workshop Electromagn., Appl. Student Innov. Competition (iWEM)*, Nanjing, China, May 2016, pp. 1–3.

[16] E. Shepeleva et al., "Integrated W-band photoconductive switches in SIW technology," *IEEE Microw. Wireless Compon. Lett.*, vol. 31, no. 7, pp. 865–868, Jul. 2021.

[17] I. Lim and S. Lim, "Substrate-integrated-waveguide (SIW) single-pole-double-throw (SPDT) switch for X-band applications," *IEEE Microw. Wireless Compon. Lett.*, vol. 24, no. 8, pp. 536–538, Aug. 2014.

[18] X. Zhao, O. Glubokov, and J. Oberhammer, "A silicon-micromachined waveguide platform with axial ports for integrated sub-THz filters," *IEEE Trans. Microw. Theory Techn.*, vol. 70, no. 2, pp. 1221–1232, Feb. 2022.